Nucleic Acids Research, 2026, **54**, gkag199
https://doi.org/10.1093/nar/gkag199
Genome integrity, repair and replication

Mitotic BLM functions are required to maintain genomic stability

Tamara Eleanore Hamann[1,†], Angela Wieland[1,2,†], Farbod Mohseni[1], Kruno Vukušić[3], Andrea Tirincsi[1], Rene Wardenaar[4], Marialucrezia Losito[4], Iris Harmsen[4], Ipek Ilgin Gönenc[5], Bernd Wollnik[5,6,7], Floris Foijer[4], Iva M. Tolić[3], Zuzana Storchová[1], Markus Räschle[1,*]

[1]Department of Molecular Genetics, RPTU University Kaiserslautern-Landau, Paul-Ehrlich Straße 24, Kaiserslautern 67663, Germany
[2]Present address: Hematology Diagnostic Laboratory MVZ Heppenheim, 64646 Heppenheim,Germany
[3]Ruđer Bošković Institute, Bijenička Cesta 54, Zagreb 10000, Croatia
[4]European Research Institute for the Biology of Ageing (ERIBA), Antonius Deusinglaan 1, Groningen 9713, The Netherlands
[5]Institute of Human Genetics, Heinrich-Düker Weg 12, University Medical Center Göttingen, Göttingen 37073, Germany
[6]German Center for Cardiovascular Research (DZHK), Partner Site Göttingen, Göttingen 37075, Germany
[7]Cluster of Excellence "Multiscale Bioimaging: from Molecular Machines to Networks of Excitable Cells" (MBExC), University of Göttingen, Göttingen 37073, Germany

*To whom correspondence should be addressed. Email: raeschle@bio.uni-kl.de
†Equal contribution.

Abstract

The BLM helicase is a critical genome maintenance protein involved in diverse cellular processes including DNA replication, repair, transcription, and chromosome segregation. During mitosis, it cooperates with the PICH helicase and topoisomerases to resolve ultrafine DNA bridges (UFBs)—nonchromatinized DNA structures that link sister chromatids—through a mechanism that is not yet fully understood. Here, we tagged endogenous BLM and PICH with fluorescent proteins and BLM with an auxin-inducible degron to generate a cell model system that enables temporal tracking of UFB dynamics in the presence or absence of BLM. Time-resolved lattice light sheet microscopy established the dynamic localization patterns of BLM and PICH throughout the cell cycle. While BLM cycles between PML bodies and DNA repair foci in interphase, these structures disappear at the mitotic entry, and BLM then re-associates with chromatin during anaphase to UFBs as well as to CENP-B-positive mitotic foci. Acute BLM depletion during mitosis increased the fraction of unresolved UFBs, micronuclei containing acentric fragments, binucleation, and resulted in subtle genomic abnormalities detected by single-cell whole genome sequencing. These findings highlight a mitosis-specific role for BLM in UFB resolution and underscore its function in preserving genomic stability.

Graphical abstract

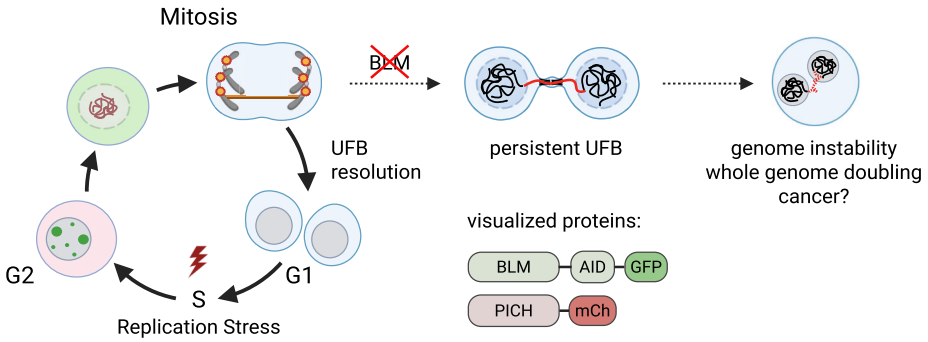

Introduction

Bloom syndrome is a rare genetic disorder characterized by developmental defects, immunodeficiency, and a strikingly high incidence of early-onset cancers [1]. It is caused by biallelic mutations of the *BLM* gene [2]. Cells of Bloom syndrome patients show features of increased genomic instability, such as elevated rates of sister chromatid exchanges (SCEs), mitotic aberrations, and chromosome breakage. The *BLM* gene encodes a highly conserved 3′–5′ ATP-dependent helicase and its expression is tightly regulated throughout the cell cycle. The abundance sharply increases at the beginning of S phase, reaching maximum levels during S and G2 phase. In late mitosis, BLM is degraded by the ubiquitin–proteasome system and remains undetectable during most of the G1 phase [3, 4]. BLM protein associates with topoisomerase 3 alpha (TOP3A) and RecQ-mediated genome instability 1 and 2 (RMI1 and

Received: May 9, 2025. **Revised:** January 31, 2026. **Accepted:** February 10, 2026

RMI2) in the so-called BTRR complex; inactivation of these interactors causes the Bloom syndrome-like disorder [5, 6]. Together, they promote strand resection as well as dissolution of recombination intermediates. In addition, BLM has been reported to facilitate the restart of stalled replication forks and the removal of secondary structures, such as G-quadruplex, in DNA and RNA (reviewed in [7, 8]).

Consistent with its multiple functions in various DNA metabolic pathways, the subcellular localization of the BLM helicase and its interaction with other proteins are highly dynamic and tightly regulated. BLM primarily localizes to membrane-free, nuclear structures called promyelocytic leukemia nuclear bodies (PML-NB) [9, 10], as well as to diffuse patches representing the nucleolus, where it likely contributes to the replication and transcription of the repetitive ribosomal DNA (rDNA) sequences [11, 12]. In S and G2 phase cells, DNA damage triggers the rapid re-localization of BLM from PML-NBs into small DNA repair foci positive for phosphorylated H2AX, and several other DNA repair proteins including RAD51 and FANCD2 [13, 14]. A subfraction of these repair foci also stains positive for the single-stranded DNA-binding replication protein A (RPA) and proliferating-cell-nuclear-antigen (PCNA), suggesting they form at sites of stalled DNA replication forks [15–17]. As cells enter mitosis, BLM becomes highly phosphorylated by PLK1, MPS1, CDK1, and other mitotic kinases, which regulates its interaction with other proteins and DNA [4, 18, 19]. In anaphase, BLM co-localizes with polo-like kinase 1 (PLK1)-interacting helicase (PICH) at so-called ultrafine bridges (UFBs) [20] that physically link the segregating sister chromatids. Transient UFBs are sporadically observed in untreated, healthy cells, indicating that their resolution is a normal physiological process essential for accurate sister chromatid segregation. Interference with DNA replication or the induction of homologous recombination strongly increases UFB formation [21]. Accordingly, UFBs are often formed within difficult-to-replicate genomic regions, or in hotspots of mitotic DNA recombination, such as common fragile sites, rDNA, telomeres, or centromeres [22, 23]. Although the exact structure of the DNA residing in UFBs remains largely unknown, different classes of UFBs have been proposed to be composed of either late replication intermediates consisting of double-stranded DNA flanked by stalled replication forks, fully replicated DNA held together by catenanes or recombination intermediates, respectively (recently reviewed in [24]). UFBs are free of nucleosomes and cannot be visualized by standard DNA dyes, suggesting that the DNA between the segregating sisters is either highly stretched or single-stranded [25]. Instead, UFBs can be identified by associated proteins, including the PICH and BLM helicases. The current model for the resolution of replication-stress induced UFBs involves the recognition of stretched DNA by the PICH helicase, followed by the recruitment of the BTRR complex and other proteins to the UFB. Subsequently, the BLM helicase unwinds double-stranded DNA, while TOP3A and TOP2A help to resolve topological structures to unlink the sister chromatids [26–29]. Taken together, the BLM helicase not only plays a crucial role in genome maintenance during S and G2, where it promotes DNA replication and recombination, but also in mitosis, where it supports effective UFB disjunction. However, to what extent the early and late functions of BLM contribute to genome stability remains largely unknown. Here, we established a cell line allowing *in vivo* visualization of UFBs through fluorescently tagged BLM and PICH. Using this cell line, we demonstrate that BLM foci are resolved before nuclear envelope breakdown (NEBD) and that the helicase is subsequently recruited "*de novo*" to UFBs during anaphase. Moreover, BLM accumulates at anaphase onset in previously uncharacterized "mitotic foci," frequently localized near centromeres. BLM depletion stabilizes UFBs and promotes genomic instability. Notably, mitosis-specific BLM depletion underscores its essential role in UFB resolution and genome maintenance during cell division.

Materials and methods

Antibodies

A lists of all antibodies used in this study is provided in Table 1.

Cas9/sgRNA plasmid construction

The Cas9/sgRNA plasmid was constructed using the px330-U6-Chimeric_BB-CBh_hSPCas9 plasmid obtained from Feng Zhang (Addgene plasmid #42230) [30]. Two oligonucleotides, each containing a target-specific guide RNA sequence of 20 nucleotides and appropriate overhangs, were cloned into the px330-based plasmid. The target-specific guide RNA sequence was selected using the Benchling tool, prioritizing sequences proximal to the stop codon with optimal off-target and on-target scores for c-terminal gene tagging.

Homology donor plasmid construction

Homology donor plasmids were generated through a multistep cloning process. First, target-specific homology arms, fluorescence markers, the 44-amino acid version of the AID tag [31] and the resistance genes were individually cloned into the linearized pIDC backbone plasmid (Geneva Biotech) to generate the pENTRY constructs using the Gibson Assembly Cloning Kit (NEB #E2611). Subsequently, homology donors were generated by combining the inserts of the pENTRY vectors with the acceptor vector pSG3651 using the NEBridge Golden Gate Assembly Kit (NEB #E1602), and error-free assembly was confirmed by DNA sequencing. The DNA insert sequences for the individual homology arms (800 bp), the AID domain, the fluorescence marker enhanced green fluorescence protein and mCHERRY were ordered as gblocks with corresponding overhangs for Gibson assembly from Integrated DNA Technologies (see Fig. 1, and Supplementary Figs S1 and 7 for details). Inserts for the hygromycin and neomycin resistance genes were PCR amplified from pMK292 (Addgene #72830) and pMK293 (Addgene #72831). All sequences are available upon request.

Cell culture, transfection, and colony isolation

The parental human colon cancer cells, HCT116 Tet-OsTIR1 ([32], a kind gift from Dr. Masato Kanemaki), were cultured in Dulbecco's Modified Eagle Medium (DMEM) with high glucose and GlutaMAX (Thermo Fisher Scientific). The medium was supplemented with 10% fetal bovine serum (FBS) (Thermo Fisher Scientific), 1% streptomycin/penicillin (Thermo Fisher Scientific), and 1 μg/ml puromycin (Thermo Fisher Scientific). The cells were maintained in a 5 % CO_2 humidified incubator at 37°C. Cells were routinely tested for the absence of mycoplasma contamination (MycoStrip, Invivogen). Plasmids and homology donors were co-transfected with

Table 1. Antibodies

Antibody	Company	Dilution	Application[a]
Mouse anti-53BP1	Millipore, MAB3802	1:500	IF
Mouse anti-α actinin	Santa Cruz, sc-17829	1:1000	WB
Rabbit anit-γH2Ax	Abcam, ab2893	1:500	IF
Mouse anti-BLM	Santa Cruz, sc-365753	1:250	WB
Mouse anti-CENP-B	Santa Cruz, sc-376392	1:1000	IF
Rabbit anti-Cyclin A2	Abcam, 181591	1:500	IF, WB
Mouse anti-Cyclin B1	Cell Signaling, 4135	1:2000	WB
Rat anti-GFP	ChromoTek, 3H9	1:250	WB
Rabbit anti-mCherry	Proteintech, 26765-1-AP	1:1000	WB
Mouse anti-MPM2	Merck, 05-368	0.06 μg	FC
Rabbit anti-PCNA (D3H8P)	Cell Signaling, 13110	1:1000	IF
Rabbit anti-PICH	Abnova, H00054821-D01	1:1000	WB
Rabbit anti-PICH	Abnova, H00054821-D01	1:150	IF
Mouse anti-PML	Santa Cruz, sc-966	1:250	IF
Rabbit-anti-RAD51	Santa Cruz, sc-8349	1:250	IF
Alexa Fluor 594 donkey, anti- mouse	Biozol, JIM-715-585-150	1:500	IF
Alexa Fluor 647 donkey, anti-rabbit	Biozol, JIM-711-605-152	1:500	IF
Alexa 488-conjugated goat anti-mouse IgG	Biozol, JIM- 115-545-003	1:300	FC
Anti-mouse HRP	R&D Systems, HAF007	1:5000	WB
Anti-rabbit HRP	R&D Systems, HAF008	1:5000	WB
Anti-rat HRP	R&D Systems, HAF005	1:5000	WB

[a]FC, flow cytometry; IF, immunofluorescence; WB, western blotting.

PEI (Polyscience) for 6 h and after 2 days, the cell suspension was distributed onto 15 cm culture plates to ensure single-cell distribution, followed by selection in medium containing 100 μg/ml hygromycin B or neomycin (both Invivogen). After 14 days, individual colonies were picked, expanded, and validated by PCR, flow cytometry, and western blotting. For PICH tagging, neomycin resistant, mCherry-positive single cells were sorted into individual wells of a 96-well plate using a SONY SH800S cell sorter and expanded in the presence of neomycin. Successful PICH tagging was validated by western blotting and Sanger sequencing. In all experiments, cells were harvested by trypsinization. Cells were centrifuged at 1300 rpm for 3 min, and cell pellets were washed once with phosphate buffered saline (PBS) and directly processed, as indicated.

Auxin-induced protein degradation and cell cycle synchronization

To induce degradation of the AID-tagged BLM protein, HCT116-Tet-OsTIR1 $BLM^{AID/GFP}$ were preincubated for at least 24 h with 1 μg/ml doxycycline to induce expression of OsTIR1, followed by incubation with 500 μM auxin (indole-3-acetic acid, IAA). For cell synchronization, cells were arrested at the G1/S boundary by addition of thymidine (2 mM final, 24 h). To release cells from the single thymidine block, cells were washed trice with warm PBS and placed into fresh media containing 100 nM APH to induce mild replication stress or dimethylsulfoxid (DMSO) as a control. For continuous BLM depletion ("S + M" depletion), auxin was added together with thymidine at the start of the cell synchronization. To restrict BLM depletion to mitosis ("M"), auxin was added at the indicated time after the release from the thymidine block. After the thymidine wash-out, media was replenished with fresh doxycycline (1 μg/ml) and auxin (500 μM) as indicated.

For scWGS analysis, 1×10^6 $BLM^{AID/GFP}$ cells were seeded per 10 cm dish and synchronized as described above, except that the cells were released into fresh media containing 10 μM EdU to monitor progression through S phase. Six hours after the release from the thymidine block, cells were washed thrice with PBS and incubated in media containing 100 nM APH to induce mild replication stress and 500 nM palbociclib (Seleck) to arrest the cells at the next G1 phase. After 18 h, the cells were harvested and fixed using 70% ethanol for flow cytometry (see below). In a parallel experiment, EdU was omitted and cells were sorted into single wells for scWGS analysis (see below).

Flow cytometry

To validate the expression of GFP-tagged BLM, asynchronous cells treated for the indicated time with IAA or ethanol were harvested. Cell pellets were resuspended in 200 μl of PBS and analyzed using the Attune™ NxT Flow Cytometer (Thermo Fisher Scientific) equipped with a 488 nm blue excitation laser and a 530/30 bandpass filter for GFP emission detection. Data acquisition and analysis were performed using FlowJo software v. 10.1 (Becton, Dickinson and Company). During analysis, cell debris and cell doublets were excluded based on forward versus side scatter parameters.

To analyse cell cycle progression, pellets of synchronized cells harvested at the indicated time points were fixed by slowly adding 500 μl of 70% ice-cold ethanol while vortexing, followed by overnight incubation at 4°C. The next day, ethanol was removed by washing the cells with PBS containing 0.25% Triton-X-100, and centrifuged at 2000 rpm for 5 min. For immunostaining, cells were incubated for 1 h at RT with 0.06 μg MPM-2 monoclonal antibody resuspended in 100 μl of PBS containing 1% BSA. After washing, cells were incubated for 30 min at RT in the dark with Alexa 488-conjugated goat anti-mouse IgG antibody diluted 1:300 in 100 μl PBS containing 1% BSA. Subsequently, cells were stained with 500 μl of FxCycle™ PI/RNase staining solution (Themo Fisher Scientific) and incubated for 30 min at RT in the dark. Measurements were taken using the Attune™ NxT Flow Cytometer (Thermo Fisher Scientific) with 488 nm blue excitation and a 530/30 bandpass filter for emission detection

of the MPM2 signal and 574/26 bandpass filter for the DNA stain propidium iodide (PI) emission detection. Data were analyzed as described above, and the fraction of cells in G1, S, G2, and M phase was quantified by applying gates to the PI and histogram plot.

To measure the incorporation of 5-Ethynyl-2'-deoxyuridine (EdU), cells were permeabilized for 15 min with Fix/Perm solution (Thermo Fisher Scientific) according to the manufacturer's instructions. After permeabilization, 1 ml of PBS was added, and the samples were centrifuged for 3 min at 1300 rpm. The supernatant was discarded, and the cell pellets were resuspended in 100 µl Perm wash (Thermo Fisher Scientific). Subsequently, 500 µl of Click-iT Reaction Mix [1 µM Eterneon Red (Baseclick GmbH), 6.6% (v/v) 1.5 M Tris (pH 8.8), 500 µM $CuSO_4$, and 100 mM ascorbic acid in PBS] was added to the samples for 20 min at room temperature in the dark. After the incubation, the samples were washed three times with 500 µl of Perm wash (centrifugation for 2 min at 1600 rpm). Finally, for DNA staining cells were incubated in 300–500 µl of PBS containing 1 µg/ml 4',6-diamidino-2-phenylindole (DAPI) and 10 µg/ml RNase. Flow cytometry was performed with an Attune™ NxT Flow Cytometer. DAPI and EdU-bound Eterneon-Red were excited by a 405 nm and a 638 nm laser, respectively. The emission from the excited DAPI was collected with a 440/50 filter. The light emitted by the excited Eterneon-Red was collected with a 670/14 filter. Data were analyzed as described above and EdU incorporation was quantified by plotting the Eterneon-Red against the DAPI intensity.

Sister chromatid exchange assay

To label sister chromatids, cells were incubated for two rounds of cell division (40 h) with 20 µM bromodeoxyuridine. At a confluency of 70%–80%, cells were treated with 400 ng/ml colcemid for 4 h prior harvesting. Cells were collected by trypsinization and centrifuged at 1300 rpm for 3 min. Cell pellets were resuspended in 46.5 mM KCl and and 8.5 mM sodium citrate ($C_6H_5Na_3O_7$) incubated for 20 min at 37°C. Fixation was performed with 3:1 methanol/acetic acid for three rounds. Fixed samples were dropped onto glass slides. After drying of the spreads overnight at RT, slides were immersed in 10 µg/ml Hoechst 33258 for 20 min. After rinsing the slides in 1× Sorensen phosphate buffer (50% 0.1 M Na_2HPO_4 and 50% 0.1 M KH_2PO_4, pH 6.8), slides were exposed to UV-A for 30 min. Slides were incubated in 2× salt sodium citrate buffer (3 M NaCl and 300 mM sodium citrate, pH 7.0) for 1 h at 50°C. Slides were further immersed in 10% Giemsa stain for 30 min at RT. Slides were washed subsequently in H_2O three times and dried overnight at RT in the dark. Vectashield Mounting Medium was used, and cover slips was Sealed with glue. Twenty-five metaphases were captured per condition. The Nikon/Andor spinning disk confocal microscope was equipped with an Andor EMCCD camera and a Nikon PerfectFocus autofocus system. A ×60 (PLAN APO, NA: 1.40, WD 0.13 mm) oil immersion objective was used. Nikon's Confocal NIS-Elements program (NIS-Elements Software, Intelligent Imaging Innovations, Denver, CO, USA) was used for instrument control, image processing, and analysis.

Quantification of DNA breaks on mitotic chromosome spreads

Synchronized cells were collected 10.5 h after the release from a single thymidine block (see above). Cell pellets were resuspended in 75 mM KCl and incubated for 15 min at 37°C. Fixation was performed by resuspending the cell pellets with 3:1 methanol/acetic acid for three rounds. Fixed samples were dropped onto glass slides. Vectashield Mounting Medium with DAPI was used to visualize the DNA. Twenty-five metaphases per replicate from three independent experiments were captured. Microscopy was performed using the ×63 oil objective of a semi-automated inverted Zeiss microscope (AxioObserver Z1). Images were acquired using SlideBook 6 (Intelligent Imaging Innovations).

Clonogenic assay

Five hundred cells per well were seeded into six-well plates. After 24 h, the cells were treated with the indicated cisplatin concentrations. Ten days after seeding, colonies were rinsed with PBS, fixed using crystal violet solution, and incubated for 20 min at room temperature. The fixative was then removed, and colonies were washed once with PBS and twice with water, followed by air-drying at room temperature. Plates were subsequently scanned or analyzed in Fiji. In Fiji, the image was converted to 8-bit, and a region of interest was drawn around a single well. The area outside the ROI was cleared, and background subtraction was performed. After adjusting the threshold, the covered area, colony count, and colony size were quantified using the "Analyze Particles" tool with a size range of 10 to infinity and a circularity range of 0 to 1.

Protein isolation, SDS–PAGE, and western blotting

For whole cell lysates, cell pellets were resuspended in RIPA buffer (50 mM Tris–HCl, pH 7.5, 150 mM NaCl, 1% NP-40, 0.5% sodium deoxycholate, 0.1% SDS, and 1 mM EDTA) supplemented with protease inhibitors (complete EDTA-free, Roche) and phosphatase inhibitors (Roche) and sonicated. The lysate was incubated for 25 min at 4°C. Protein concentration was determined using the Pierce BCA Protein Assay Kit (ThermoFisher, #23225). Equal amounts of protein were resuspended in 1× Laemmli buffer [62.5 mM Tris–HCl (pH 6.8), 2% SDS, 10% glycerol, 0.01% bromphenol blue, and 1% β-mercaptoethanol], denatured for 5 min at 95°C and separated by sodium dodecyl sulfate–polyacrylamide gel electrophoresis. Proteins were transferred onto a nitrocellulose membrane (GE Healthcare). Protein transfer was validated by Ponceau S staining. Next, membranes were blocked for 1 h in 3% BSA in TBS (only for detecting BLM) or with 5% skim milk in TBST (Tris-buffered saline with 0.1% Tween 20) TBS-T, followed by overnight incubation at 4°C in primary antibodies. On the next day, the membranes were washed and incubated for 1 h in secondary antibodies at RT. Proteins were visualized with enhanced chemiluminescence (ECL) reagent (Bio-Rad) and scanned on an Azure c300 imaging system (Azure Biosystems). Protein normalization was performed using housekeeping proteins. Signal intensities were quantified using the software Fiji (National Institutes of Health).

Immunofluorescence staining

Cells were cultured on cover slips placed in six-well plates. The cells were fixed with ice-cold 100% methanol for 10 min on ice or with 4% paraformaldehyde (PFA) for 20 min at room temperature. Both fixing reagents were removed by washing the cells thrice with PBS. To permeabilize the cells, 0.5% Triton 100-X diluted in PBS was added for 20 min. Afterward, the cells were washed thrice with PBS, and then blocked

(3% BSA, 1% NaN_3, diluted in PBS-T) for 1 h at room temperature. To stain for the protein of interest, the cells were incubated with the respective primary antibodies overnight at 4°C. The following day, the cells were washed thrice with PBS and then incubated in the appropriate secondary antibody for 1 h in the dark at room temperature. After removing unbound secondary antibodies by washing with PBS, the DNA was stained by incubating the cells for 5 min with 0.2 μg/ml DAPI, diluted in PBS. For BLM visualization, the endogenous GFP signal was detected at a wavelength of 488 nm without antibody staining. The cells were washed once with PBS and once with water before mounting the cover slips on glass slides. Images were captured using the ×40 or ×60 oil objective of the Eclipse Ti2-E with Spectra III epifluorescence microscope (Nikon). For the detection of anaphase cells, z-stacks were captured with relative offsets with 25 steps and a size of 0.3 μm, range 7.2 μm. The images were analyzed manually using the software Fiji.

Live cell imaging

Live-cell imaging was performed as described [33]. Multiple 3.5 cm glass-bottom dishes were seeded at various densities. Cells that reached approximately 70% confluency were chosen to be imaged. Before imaging start the cells were stained with 30 nM of the nuclear stain SPY555-DNA (λ_{abs} 555 nm) at 37°C. Additionally, 1 μM Verapamil was added to prevent dye efflux. The cells were placed in a humidified chamber with 5% CO_2 at 37°C. Images were taken every 2 min for a minimum of 12 h using Lattice Light Sheet 7. The images were analyzed manually using the software Fiji. For tracking individual cells or foci the Fiji plugin TrackMate was used.

Statistical analysis

Data were analyzed using GraphPad Prism (version 9.0). All fluorescent images were blind counted and statistical comparisons between two groups were performed using an unpaired two-tailed Student's *t*-test. *P*-values of <0.05 were considered statistically significant and are shown on the graphs. The number of independent biological replicates (*n*) and the total number of cells or events analyzed are indicated in the figure legends. For protein co-localization analysis, Pearson correlation coefficients were calculated using the Fiji plugin Coloc 2.

scWGS and AneuFinder analysis

Sequencing was performed using a NextSeq 500 machine (Illumina; up to 77 cycles single end). The generated data were on beforehand demultiplexed using sample-specific barcodes and changed into fastq files using bcl2fastq (Illumina; version 1.8.4). Reads were afterward aligned to the human reference genome (GRCh38/hg38) using Bowtie2 (version 2.2.4, [34]). Duplicate reads were marked with BamUtil (version 1.0.3, [35]). The aligned read data (bam files) were analyzed with a copy number calling algorithm called AneuFinder (version 1.14 and 1.30, https://github.com/ataudt/aneufinder, [36]). Following GC correction and blacklisting of artefact-prone regions (extreme low or high coverage in control samples), libraries were analyzed using the dnacopy and edivisive copy number calling algorithms with variable width bins (average binsize = 1 Mb; step size = 500 kb). Blacklists and variable width bins were constructed with the use of an euploid reference [37]. Results were afterward curated by requiring a minimum concordance of 90% between the results of the two algorithms. Libraries with on average <10 reads per chromosome copy of each bin (2- somy: 20 reads, 3-somy: 30 reads, etc.) were discarded. This minimum number of reads comes down to roughly 55 000 for a diploid genome. The copy numbers of the T24 samples (T24 CTR, T24 M, and T24 S + M) were expressed relative to the median (consensus) copy number profile of the T0 control sample (T0 CTR) in order to account for the non-euploid nature of this cell line. This median copy number was determined for each bin (median across libraries). The copy numbers of this consensus copy number profile were doubled when compared to tetraploid libraries.

Calculation scores

Aneuploid scores for each sample were first calculated for each library by calculating the average absolute difference from the median copy number profile of the T0 control sample. The size of the bins was used as weight (weighted average). The genome-wide scores were calculated as the average of all the libraries of the sample. The heterogeneity score of each bin was calculated as the proportion of pairwise comparisons (cell 1 versus cell 2, cell 1 versus cell 3, etc.) that showed a difference in copy number (e.g. cell 1: 2-somy and cell 2: 3-somy). The heterogeneity score of each sample was calculated as the weighted average of all the bin scores (size of the bin as weight). The structural score of each library was simply calculated as the average number of copy number transitions (break points) divided by one million. The genome-wide scores were calculated as the average of all the libraries of the sample. For fragment size analysis copy number segments with a maximum size of 10 Mb were selected. The segments were required to show a copy number that is different from the median (consensus) copy number.

Results

Rapid degradation of BLM impairs genome stability

To study the distinct functions of BLM during different cell cycle phases, we modified the endogenous *BLM* by a c-terminal fusion with an auxin-inducible degron (AID) domain for rapid degradation of the protein [38]. In addition, eGFP was included for tracking the endogenous BLM protein in live cells. CRISPR–Cas9 knock-ins require homology donors, in which inserts are flanked by two homologous regions matching the genomic sequence at the target site. In HCT116 cells, homology arms of at least 500 base pairs (bp) are required for efficient tagging [39]. To this end, we developed a modular cloning system, in which targeting vectors can be assembled from interchangeable parts by PCR-free Golden Gate Assembly (Fig. 1A, and Supplementary Fig. S1A and B). This allows to easily combine a degron domain with different fluorescence markers (e.g. eGFP and mCherry) and resistance genes (e.g. hygromycin ($Hygro^R$) or neomycin (Neo^R). For BLM tagging, a homology donor was assembled from the AID, eGFP and $Hygro^R$ entry vectors joined by two flanking homology arms of 800 bp matching the sequence to the left and right of the stop codon in the endogenous *BLM* gene (Fig. 1A). CRISPR–Cas9-mediated gene editing was carried out with a single guide RNA targeting the Cas9 endonuclease to cut 12 nucleotides upstream of the *BLM* stop codon (Supplementary Fig. S1C). A plasmid expressing the guide RNA and Cas9 was transiently transfected into HCT116–OsTIR1 cells together with the homology donor (Fig. 1A and

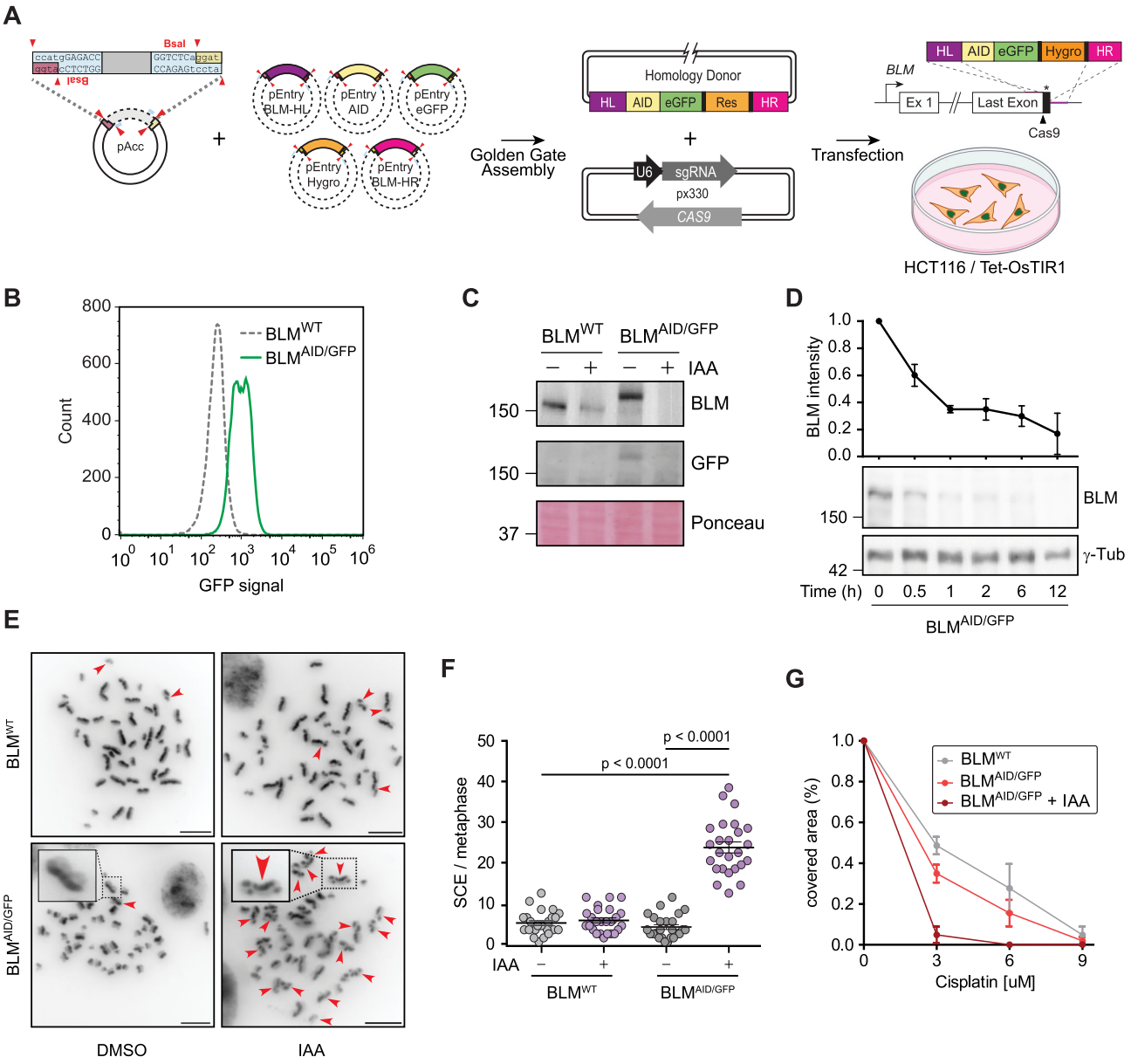

Figure 1. Endogenous AID-eGFP tagging of BLM facilitates its rapid degradation. (**A**) Schematic illustration of the gene editing strategy. (**B**) Flow cytometry showing the GFP signal in parental HCT116 and tagged BLM$^{AID/GFP}$ cells. (**C** and **D**) Immunoblotting of the lysates from parental HCT116 and BLM$^{AID/GFP}$ cells with and without auxin treatment (IAA) for 24 h (C) or as indicated (D). Proteins were detected with the indicated antibodies, Ponceau S staining served as loading control. (**E**) SCE visualized on metaphase spreads. Asynchronous HCT116 or BLM$^{AID/GFP}$ cells were incubated with IAA or DMSO for two rounds of replication. Red arrows point to metaphase chromosomes containing SCEs; insets show representative examples. (**F**) Quantification of SCE. 25 metaphase spreads were quantified for each condition, each dot represents an individual metaphase spread; mean with S.E.M., Student's *t*-test. (**G**) Sensitivity to cisplatin quantified by clonogenic assay. Mean of three independent replicates ($N = 3$) with SD is shown.

Supplementary Fig. S1D). Flow cytometry and western blotting with antibodies against GFP and BLM confirmed successful homozygous tagging in one clone, here referred to as BLM$^{AID/GFP}$ (Fig. 1B and C). Exposure of asynchronous cells to auxin for 24 h reduced the levels of the AID-tagged BLM protein to below detectable levels (Fig. 1C) and time-course experiments revealed rapid depletion of BLM with a fast drop within the first hour after auxin addition (Fig. 1D). Loss of BLM is associated with a hallmark genomic instability phenotype known as SCE [40]. Consistently, the addition of auxin to the BLM$^{AID/GFP}$ cells increased the rate of SCE events 5-fold compared to untreated control cells (Fig. 1E and F). Importantly, in the absence of auxin, SCE levels were comparable to those observed in the parental HCT116 cells with or without auxin treatment. We therefore conclude that AID-mediated depletion of BLM mimics the phenotype of BLM loss observed in cells from patients with Bloom syndrome. Furthermore, cisplatin sensitivity of cells expressing the tagged BLM helicase was comparable to the parental HCT116 cell line and increased significantly only upon BLM depletion (Fig. 1G, and Supplementary Fig. S2A and B). Together, these results confirm that the AID/GFP-tagged BLM protein is fully functional and efficiently suppresses the resolution of recombination intermediates that give rise to SCEs.

Dynamic localization of the BLM helicase in mitotic cells

First, we examined BLM localization dynamics during the cell cycle. To this end, we performed live cell imaging of asynchronous $BLM^{AID/GFP}$ cells with captures every 2 min using Lattice light sheet microscopy [33]. To induce mild replication stress, cells were incubated with the polymerase inhibitor aphidicolin (APH) at a low concentration of 100 nM for 12 h before imaging the live cells to ensure that all captured mitotic $BLM^{AID/GFP}$ cells had passed through a perturbed S phase (Fig. 2A). Notably, the low dose of APH induced mild replication stress without triggering a cell cycle arrest [41]. Live cell imaging revealed a recurrent pattern of the BLM–GFP protein on chromatin (Fig. 2B, Movie M1A and B). In S and G2 phase, before the chromosome condensation started, we observed a diffused chromatin signal of BLM–GFP, as well as several more prominent foci (Fig. 2B, and Supplementary Fig. S3A and B). The foci were confirmed to largely represent PML-positive nuclear bodies (PML-NB), as the BLM signal strongly co-localized with the PML signal in G2 phase cells (Supplementary Fig. S3C and D). In interphase, the BLM signal also partly colocalized with the DNA repair markers RAD51 and 53BP1, likely in the previously observed repair foci (Supplementary Fig. S3E–H) [13, 42]. Strikingly, the G2 BLM foci disappeared shortly before nuclear envelope breakdown (NEBD) (Fig. 2B, and Movie M1A and B), and the BLM signal became diffuse and dropped in intensity both with and without replication stress (Fig. 2C). In anaphase, the BLM–GFP protein was newly recruited to UFBs (Fig. 2B). Surprisingly, we also observed *de novo* formation of BLM foci on mitotic chromatin in late anaphase that persisted till the end of telophase, hereafter referred to as M-foci (Fig. 2B, see also Movie M2 and Supplementary Fig. S3G). To analyze the dynamic pattern of BLM–GFP localization, we tracked the mean intensity of individual foci over time, aligning all foci tracks at the NEBD (Fig. 2D). This detailed analysis further confirmed that all BLM-positive foci disappeared shortly before NEBD, irrespective of replication stress, and that in a fraction of cells, BLM-positive foci and UFBs formed *de novo* in anaphase.

We next compared the number of BLM-foci and UFBs in control and APH-treated cells captured by live-cell imaging (Fig. 2E–G). Unstressed $BLM^{AID/GFP}$ cells contained on average one G2 foci per cell, and after induction of mild replication stress, the number increased about 5-fold (Fig. 2E). Only 1% of unstressed cells contained a visible UFB and less than one M-foci, while mild replication stress increased the fraction of UFB containing cells to 13% on average, and the number of M-foci 5-fold (Fig. 2F and G). Additionally, mild replication stress increased the number of cells with co-occurring M-foci and UFBs 6-fold compared to untreated control (Fig. 2H). To further characterize the transient M-foci, we tested co-localization with PML or with the DNA repair markers γH2AX, RAD51, and 53BP1. In M-foci, BLM co-localized neither with PML nor with 53BP1 or RAD51, although there was a clear co-localization observed in G2 phase, suggesting that M-foci of BLM helicase represent a different physiological function (Supplementary Fig. S3C–F). Additionally, we observed only a limited overlap between the BLM M-foci and γH2AX in non-treated mitotic cells and only a marginal increase of the Pearson correlation coefficient from 0.31 to 0.37 upon treatment with 100 nM APH (Supplementary Fig. S3H and I). Since the BLM helicase was recently proposed to contribute to centromere stability in mitosis [27, 43], we stained the kinetochores with CENP-B antibody to evaluate the co-localization with the BLM signal (Fig. 2I and J). Strikingly, a large fraction of the BLM signal in the M-foci was next to, or overlapping with, the CENP-B signal in anaphase and telophase, while no overlap was observed in interphase, prophase, and metaphase (Fig. 2I and J, and Supplementary Fig. S3J). Taken together, the dynamic localization patterns of the endogenous BLM reveal a *de novo* recruitment of the DNA helicase in mitosis to UFBs, as well as to novel M-foci.

Both interphase and mitotic BLM functions contribute to the maintenance of genome stability

Given that BLM helicase is newly recruited to chromatin in mitosis, we asked whether restricting BLM depletion to M phase only would cause a similar phenotype as the continuous depletion across the entire cell cycle. Based on the cell cycle profile of cells synchronized by a single thymidine block, we selected the time point for cell phase-specific BLM depletion (Fig 3A and B, Supplementary Fig. S4A and B). Adding auxin 5 h after the release from thymidine block led to a gradual decrease of the BLM signal, with <10% left at 10.5 h, when most cells reached mitosis (Fig. 3C and D). With this treatment, referred to as "M" depletion, cells undergo S phase in the presence of BLM helicase, while in mitosis BLM is depleted. Additionally, we treated the cells with auxin for the entire course of the experiment, hereafter referred to as S + M depletion (Fig. 3C and D). We also attempted to restrict the depletion of the BLM helicase to S phase only by washing out auxin 5 h after the release from the thymidine block. However, there was no detectable recovery of the BLM protein (Fig. 3C and D), and therefore, we did not continue with these experiments. To rule out that M depletion impairs early BLM functions, we quantified the effect of BLM depletion on the formation of SCE events, which arise during the repair of replication-associated DNA damage by inter-sister recombination in late G2 and in prophase [18]. As expected, S + M depletion of BLM increased SCE events on metaphase arrested chromosomes 2- to 3-fold, whereas M depletion showed little effect (Supplementary Fig. S5A–C). Thus, the applied M depletion scheme preserves most of the BLM activity in late G2 and possibly even early mitosis.

We next analyzed mitotic aberrations in cells released from thymidine block into media with or without APH. We first quantified micronuclei, which harbor broken or mis-segregated chromosomes [44]. In the absence of replication stress, S + M depletion of BLM caused a 5-fold increase in micronucleated cells, while M depletion caused a 2-fold increase. Replication stress led to an additional increase in micronucleation in all cases (Fig. 3E). 95% of micronuclei contained a broken chromosome, as evidenced by the lack of staining with anti-CENP-B antibody, a marker of the inner kinetochore (Fig. 3F). Together, this suggests that the damage leading to micronuclei in these cells arises largely in S phase. Because the majority of micronuclei contained a fragment of a broken chromosome, we next quantified aberrations on metaphase chromosomes. S + M depletion of BLM led to a 2-fold increase of breaks and gaps (Fig. 3G), which likely coincide with sites of mitotic DNA synthesis (MIDAS) [45]. In contrast, M depletion resulted in a much smaller increase of mitotic chromosomes with aberrant morphology. While mild replication stress increased gaps and breaks about 3-fold in control cells, BLM depletion surprisingly did not further exacerbate this

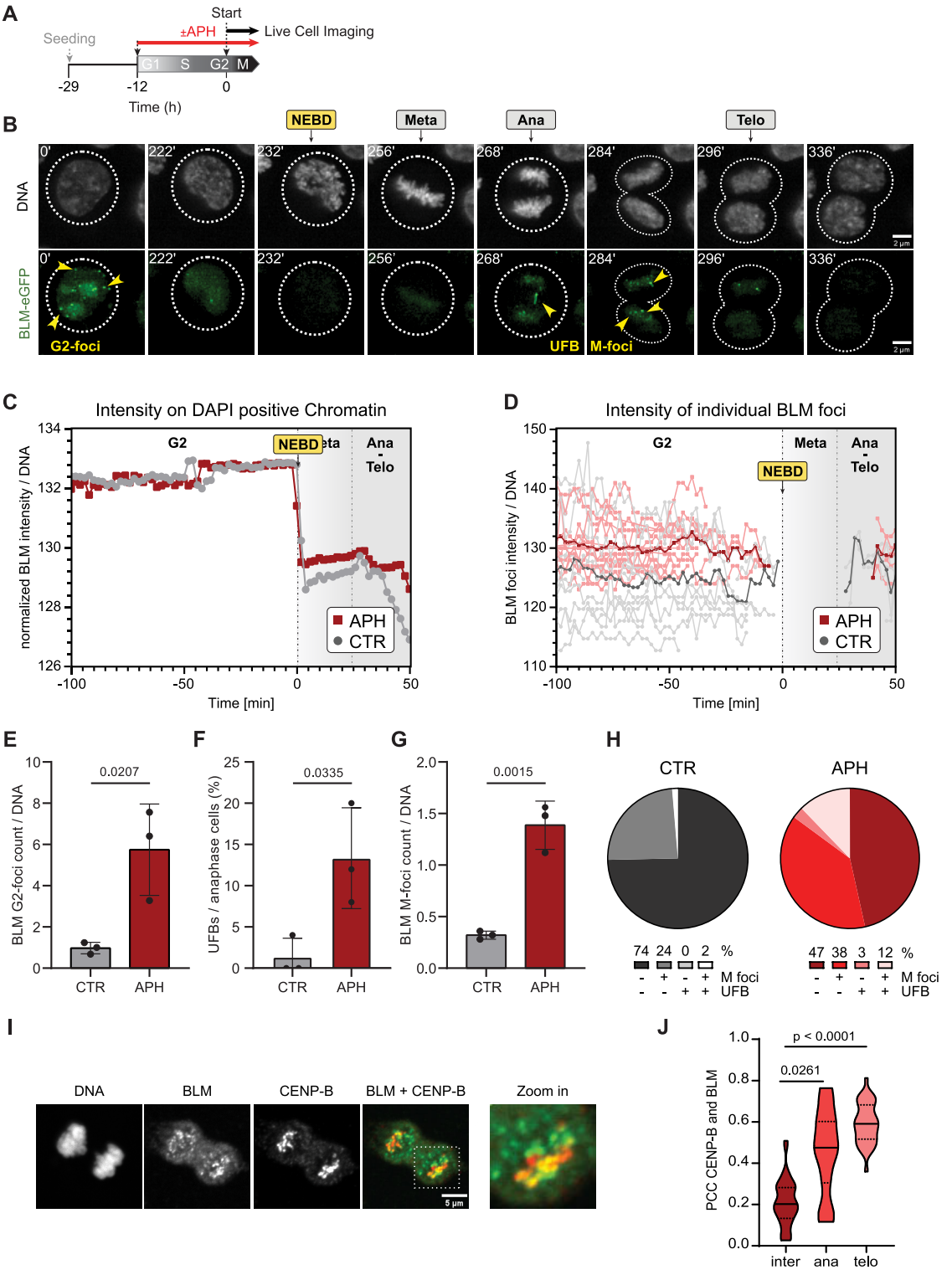

Figure 2. Endogenous BLM shows bimodal recruitment to chromatin. (**A**) Experimental scheme. APH, aphidicolin. (**B**) Representative stills taken from live cell imaging of $BLM^{AID/GFP}$ cells treated with 100 nM APH, showing progression from G2 phase to mitotic exit with UFB and M-foci in ana-/telophase. White dotted circles indicate the cell of interest; yellow arrows mark BLM positive G2-foci, M-foci, or UFBs; scale bar: 5 µm, the time (min) relative to the start of the movie is indicated on the top left corner. See Supplementary Movie S1A. DNA was labeled with SPY 555. (**C**) Mean BLM–GFP intensity on chromatin over time tracked in individual cells (15 cells per biological replicate, $n = 3$) using TrackMate (Fiji plugin), aligned at NEBD (timepoint 0), and normalized to the untreated control (CTR). (**D**) Intensity of individual BLM–GFP foci over time, tracked as in (C) (5 cells per replicate, $n = 3$). NEBD, nuclear envelope breakdown; Met, Metaphase; Ana, Anaphase; Telo, Telophase. (**E–G**) Percentage of cells with G2 foci (E), BLM positive UFBs (F), or M-foci (G). (**H**) Percentage of cells with no foci, only M-foci, only BLM positive UFBs, or both. Panels (E–H) show data from 25 cells per biological replicate ($n = 3$), mean ± SD is shown. For the analysis of BLM foci, a threshold was set based on APH-treated cells. The same threshold was used for G2- and M-foci. Live cell imaging was performed with a Lattice Light Sheet 7 microscope. (**I**) Representative microscopy images of BLM and CENPB co-localization in mitotic cells. (**J**) Pearson correlation coefficient of BLM and CENP-B signals. Mean and quantiles are shown as a dotted line. 25 cells per biological replicate were evaluated, $n = 3$.

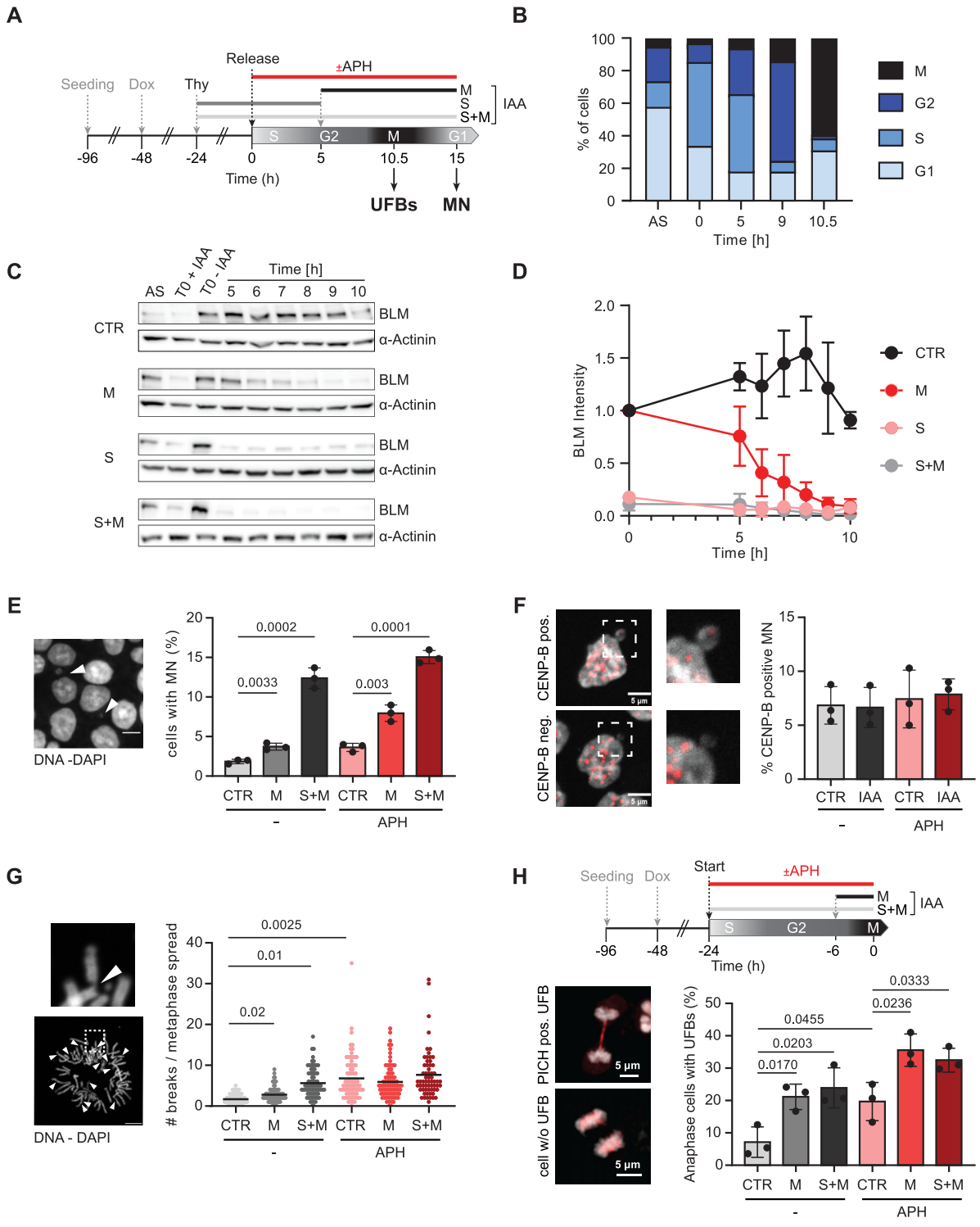

Figure 3. BLM depletion restricted to mitosis increases mitotic aberrations. (**A**) Experimental scheme. UFB, ultrafine bridges; MN, micronuclei; APH, aphidicolin; IAA, auxin; Thy, thymidine; Dox, doxycycline. (**B**) Cell cycle profile of $BLM^{AID/GFP}$ cells released from a single thymidine block. AS, asynchronous control. M phase was determined by staining with an MPM2 antibody, see Supplementary Fig. S4A. (**C**) Representative immunoblots of BLM in cells after release from single thymidine block with IAA added at specific timepoints as shown in panel (A). α-Actinin serves as loading control. CTR, control (no IAA); M, IAA added at 6 h after the release, S, IAA added at the synchronization start and washed out 6 h after the release, S + M, IAA added at the synchronization start; AS, asynchronous cells. (**D**) Quantification of the BLM abundance from panel (C), normalized to the timepoint 0. (**E**) Percentage of cells in the subsequent G1 (15 h after release from the single thymidine block) with micronuclei (MN). Cells were treated as shown in (A), except that auxin was added 6 h after the thymidine release. Student's *t*-test, mean ± S.E.M.; >400 cells per replicate; three independent experiments. (**F**) Fraction of CENP-B positive micronuclei (MN) in asynchronous $BLM^{AID/GFP}$ cells with or without treatment with IAA for 24 h. Student's *t*-test, mean ± SD is shown, $n = 3$. (**G**) Chromosome spreads from cells harvested 10.5 h after the release from single thymidine block. Cells were treated as shown in (A), except that auxin was added 6 h after the thymidine release. Chromosome breaks were counted in 25 metaphase cells per replicate, three independent experiments, mean ± S.D. is shown. (**H**) Fraction of cells with PICH-positive UFBs in asynchronous cells treated for 24 h with APH. IAA was added together with APH (S + M depletion) or 6 h before harvesting (M depletion). Student's *t*-test, mean ± SD is shown, three biological replicates.

phenotype. We hypothesize that even a low concentration of APH (100 nM) may damage some cells so severely that they become delayed or arrested in G2. Consistent with this notion, ~25% of APH treated cells showed a small G2/M peak that persisted until 14 h after the release from the thymidine block, while most DMSO-treated cells had entered already the next cell cycle at this time (see Supplementary Fig. S4B).

Unlike the mild effects on the formation of SCE, micronuclei or chromosomal gaps and breaks, mitotic depletion of BLM led to a robust increase of anaphase cells with PICH positive UFBs (Fig. 3H) or chromatin bridges (Supplementary Fig. S6A–C). Notably, BLM depletion over the entire cell cycle did not cause any further significant increase of UFBs or chromatin bridges. Exposure of the cells to mild replication stress further elevated the formation of UFBs, but the effect of BLM depletion remained similar. Collectively, the results suggest that the BLM protein plays an essential role during M phase by suppressing the occurrence of UFBs, chromatin bridges and lagging chromatin through mechanisms that are largely independent of its S phase functions.

Visualization of replication stress-induced UFBs in BLM-depleted cells reveals persistent sister chromatid linkages

To study the effect of BLM depletion on UFB resolution by live cell imaging, we additionally tagged the PICH protein with mCherry in the $BLM^{AID/GFP}$ cells (Fig. 4A and Supplementary Fig. S7A–D). mCherry-positive cells were sorted by flow cytometry, and single cell clones were validated by western blotting with antibodies against mCherry and PICH for homozygous tagging (Supplementary Fig. S8A). In the double-tagged cell line, the PICH-mCherry signal localized diffusely in the cytosol of interphase cells and rapidly re-localized to chromatin upon NEBD, as previously reported [25, 26] (Supplementary Fig. S8B and C, Movie M3A and B). On mitotic chromatin, a weak PICH-mCherry signal was observed along all chromosomes. As soon as the cells entered anaphase, bright PICH-positive foci and UFBs appeared transiently in a subset of cells. Within these foci, and on UFBs, the PICH and BLM signals colocalized with high correlation (Fig. 4B and C, see also Movie M3A and B). Notably, using antibodies for indirect immunofluorescence detection in the same cell, a strong PICH signal was observed along the BLM-positive UFBs, whereas the localization to M-foci was much less apparent, possibly due to high background signal observed with the PICH antibody (Fig. 4B, lower row). A similar depletion of the PICH signal on condensed chromosomes in immunofluorescence experiments has also previously been observed (e.g. [46, 47]). We speculate that this might be either due to post-translational modifications interfering with antibody binding or due to a general inaccessibility of the epitope within the condensed chromatin. Taken together, endogenous tagging of BLM and PICH revealed highly correlated mitotic signals both on UFBs and M-foci.

Using the $BLM^{AID/GFP}$/$PICH^{mCherry}$ double-tagged cell line, we analyzed the consequences of BLM depletion on UFBs by live cell imaging under mild replication stress. Consistent with the results obtained with fixed cells (compare Fig. 3H and Supplementary Fig. S6C), BLM depletion led to a small, but significant increase of mitotic cells with PICH positive UFBs (Supplementary Fig. S8D). PICH localized to UFBs both in the presence and absence of BLM, further supporting its upstream role in the recruitment of the BLM helicase and other proteins to UFBs, as previously suggested [20, 47]. Interestingly, BLM depletion also prolonged the lifetime of UFBs by about 4 min on average (Supplementary Fig. S8E), whereas the time for the passage from the start of anaphase to the mitotic exit remained unchanged (Supplementary Fig. S8F). Careful tracking of anaphase across multiple time frames revealed two distinct classes of PICH-positive UFBs (Fig. 4D). In the first class, UFBs appear as a straight line of the PICH signal, which disappears from the middle to the sides within a few minutes (Fig. 4D, upper panel, "straight" UFBs, Movie M4A and B). In the second class, the originally "straight" UFBs became "wavy" in the later stages of mitosis, and the PICH signal dissipated into a small number of foci along the path of the UFB before disappearing (Fig. 4D, lower panel, Movie M5A and B).

Intriguingly, upon depletion of the BLM helicase, only the fraction of the "wavy" UFBs increased more than two-fold compared to BLM positive cells, while the "straight" UFBs appeared unaffected (Fig. 4E). Strikingly, the PICH signal on the "wavy" UFBs was present twice as long than on the "straight" UFBs (20 versus 10 min, Fig. 4F). Thus, most of the "straight" UFBs were dissolved before chromatin decondensation started, while "wavy" UFBs were still observed in telophase (compare Fig. 4D, upper and lower panel). It is important to consider that the loss of the PICH signal toward the end of anaphase does not necessarily mean that the linkage between the sister chromatids has been resolved. We therefore hypothesized that these unresolved DNA bridges might interfere with cytokinesis, giving rise to binucleated cells. Indeed, we observed a significant increase in binucleated cells upon BLM depletion in fixed cells, which was further exacerbated by mild replication stress (Fig. 4G). These results suggest that the loss of BLM function leads to increased occurrence of "wavy" ultra-fine bridge structures, which take longer to resolve. Unresolved "wavy" UFBs may thus contribute to the formation of binucleated cells, leading to whole genome doubling and potentially promoting aneuploidy and cancer.

To corroborate these findings, UFBs were analyzed in fixed cells and quantified separately for anaphase and telophase (Fig. 5A–C). Strikingly, while BLM depletion had little effect on the fraction of UFBs in anaphase cells (Fig. 5D), it significantly increased the fraction of UFBs in telophase (Fig. 5E). Because continuous or mitotically restricted BLM depletion increased the fraction of UFB-containing telophase cells to a similar extent, we conclude that BLM's mitotic function directly contributes to UFB resolution.

Single-cell sequencing uncovers genomic instability and whole genome doubling after BLM depletion

Next, we performed single-cell whole genome sequencing (scWGS) to define genomic copy number alterations (CNAs) in BLM-depleted cells that progressed through one cell cycle in the presence of mild replication stress. To this end, we synchronized cells by a single thymidine block and released them into media with or without 100 nM APH (Fig. 6A). The BLM helicase was either depleted throughout the entire experiment (S + M), or only during M phase. At the release, we added EdU to label DNA in replicating cells, and after 6 h, the CDK4/6 inhibitor palbociclib to trap the cells in the subsequent G1 to

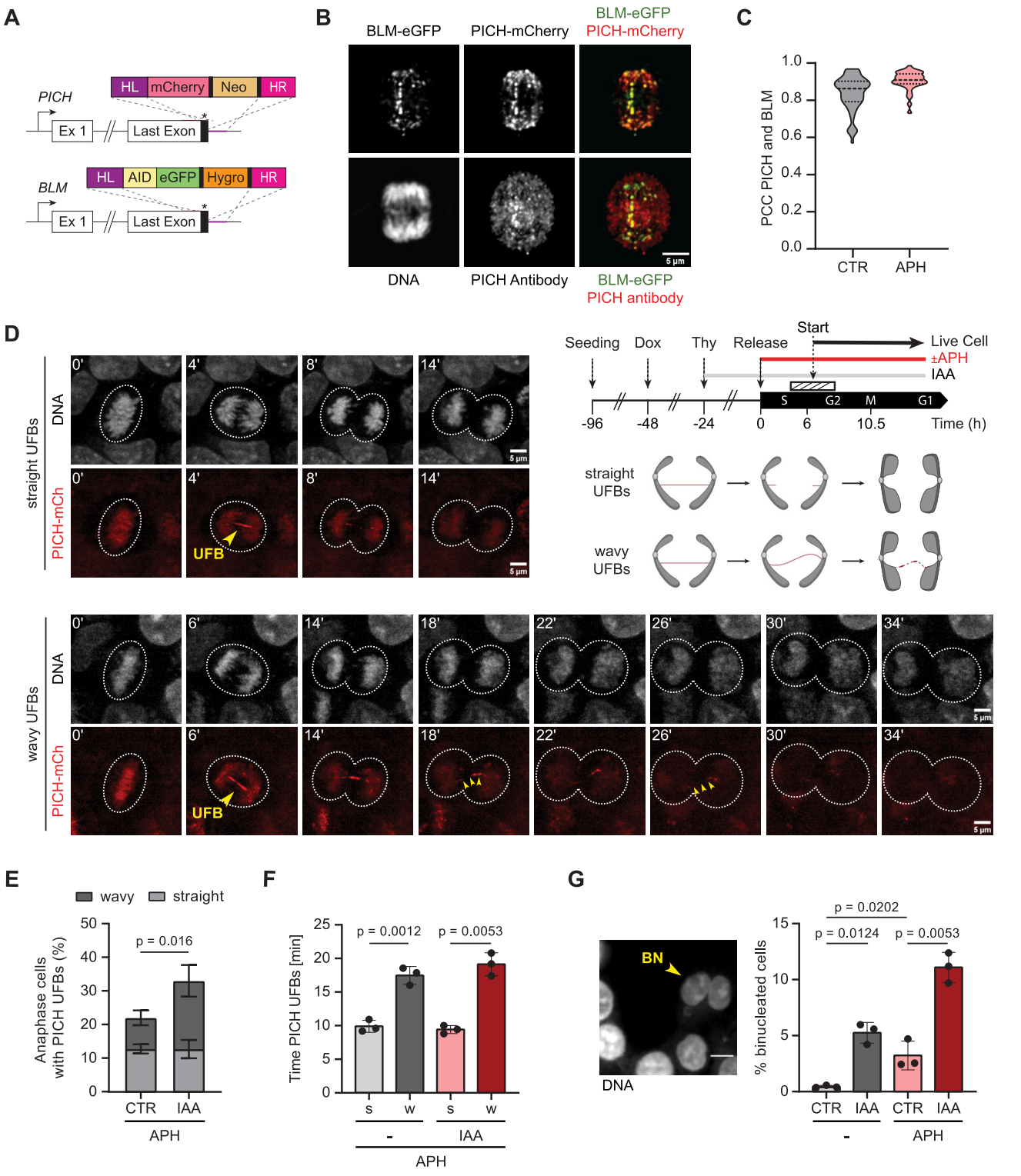

Figure 4. Visualization of replication stress-induced UFBs in BLM-depleted cells reveals persistent sister chromatid linkages. (**A**) Schematic illustration of the gene editing strategy in BLM$^{AID/GFP}$ cells. Imaging was started ~6 h after the released from a single thymidine block (hashed bar). (**B**) Representative microscopy image of a fixed anaphase cell. BLM was visualized with the GFP tag, PICH was visualized either by an antibody or by direct mCherry fluorescence detection, and DNA was stained with DAPI. (**C**) Pearson Correlation coefficient for the eGFP and mCherry signal in the nucleus. Data from 75 cells were pooled from three independent experiments for each condition. (**D**) Representative still images of cells synchronized and treated as in (C) and a schematic illustration of the live cell imaging strategy. The UFBs were visualized with PICH-mCherry, and DNA was stained with SPY555. The cartoon depicts the two different fates of UFBs; scale bar: 5 μm; UFB, ultrafine bridges; MN, micronuclei; APH, auxin; IAA, auxin;Thy, thymidine; Dox, doxycycline. (**E**) Quantification of the UFBs detected by live cell imaging (panel C). CTR, control; IAA, auxin. Student's *t*-test, mean ± SD is shown, $n = 3$. (**F**) Duration of the PICH-mCherry signal along UFBs shown separately for "straight" (s) and "wavy" (w) UFBs. Student's *t*-test, mean ± SD is shown, $n = 3$. For each replicate, 25 cells were tracked in live cell movies as shown in (D). A detailed cell treatment scheme is provided in (C). (**G**) Quantification of binucleated cells. Cells were fixed 15 h after release from a single thymidine block. IAA was added together with thymidine at the start of the synchronization and kept throughout the course of the experiment. Student's *t*-test, mean ± S.E.M.; > 200 cells per replicate ($N = 3$); scale bar, 10 μm.

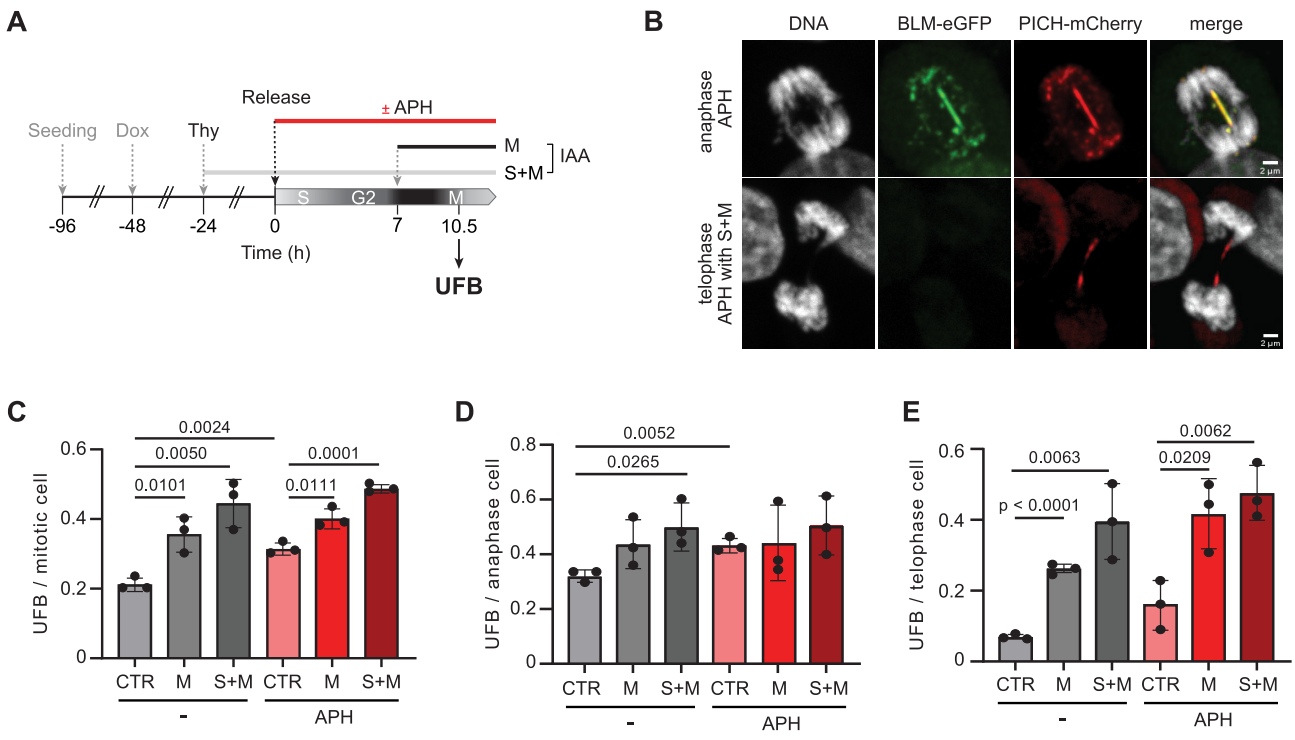

Figure 5. BLM depletion increases the fraction of long-lasting UFBs that persist until telophase. (**A**) Schematic illustration of the experimental setup. (**B**) Representative microscopy image of fixed cells in anaphase or telophase treated with IAA as indicated. BLM and PICH were visualized via the fluorescence of eGFP or mCherry, respectively; DNA was stained with DAPI. (**C**) Quantification of the fraction cells containing UFBs in all mitotic cells. (**D**) Quantification of UFBs in anaphase cells. (**E**) Quantification of UFBs in telophase cells. Student's *t*-test, mean ± SD is shown, $n = 3$. For each replicate 30 cells were analyzed.

obtain homogenous populations for scWGS. Flow cytometry confirmed that more than 85% of the cells were trapped in G1, after going through replication during the last 24 h (Supplementary Fig. S9A and B).

As expected, genomes of cells analyzed at the time of release (T0) showed only a low level of chromosomal aberrations, confirming that HCT116 is a chromosomally stable cell line (Fig. 6B) [48]. In contrast, passage through only a single cell cycle in the presence of mild replication stress caused a significant increase of genomic aberrations defined by the number of CNAs (Fig. 6C). Quantification of aneuploidies and CNAs using the Aneufinder algorithm [36] revealed a 2- to 3-fold increase of aneuploidy and sample heterogeneity, whereas structural aberrations remained largely unchanged (Fig. 6D). Although BLM depletion did not significantly alter aneuploidy or the frequency of structural aberrations, it modestly increased sample heterogeneity and led to an accumulation of tetraploid cells (Fig. 6E). To robustly quantify the heterogeneity of CNAs, we removed all technical artifacts (see Materials and methods) and normalized the read counts of T24 samples to the median of T0 controls, which were harvested prior to the release into S phase (Supplementary Fig. S10A–C and Supplementary Fig. S11A–C). To exclude CNAs involving entire chromosome arms, we filtered the dataset to retain only CNAs shorter than 10 Mb (see Materials and methods). Although this refined analysis revealed no statistically significant differences in the heterogeneity scores among T24 samples (Supplementary Fig. S10D–F and Supplementary Fig. S11D–F), BLM-depleted samples displayed a significant reduction of the median CNA fragment length from 4.4 to 3.2 Mb (Fig. 6F). Collectively, the scWGS data indicate that BLM depletion leads to an accumulation of tetraploid cells and a shift toward shorter-sized CNA fragments, supporting the notion that, in the absence of BLM, a subset of replication intermediates is resolved through an alternative pathway or not resolved at all.

Discussion

The BLM helicase supports many different facets of DNA metabolism. While the BLM functions during the S and G2 phase in DNA replication and homologous recombination-mediated repair have been extensively studied and well established, its roles in mitosis remain poorly understood. By establishing a cell line that allows live cell imaging of the BLM and PICH helicases along with an acute and efficient BLM depletion, we demonstrate that BLM has distinct functions during M phase that are essential for maintaining genome stability. Live cell imaging revealed a remarkably dynamic localization of the BLM and PICH helicases throughout the cell cycle. Most strikingly, we observed that the focal accumulation of BLM colocalizing with PML and DNA repair foci in interphase is completely resolved when cells undergo NEBD that is driven by a peak in cell cycle kinase activity [49]. Intriguingly, mitotic phosphorylation of BLM has previously been suggested to promote its exclusion from chromatin, as indirectly shown by biochemical fractionation [3]. As cells progress into anaphase, our live cell imaging analysis reveals a *de novo* recruitment of BLM to ultrafine bridges as well as a few discrete mitotic foci (Fig. 2B–D). The precise regulatory mechanisms that enable a subset of BLM helicase to restore its binding to chromatin during anaphase and to control its

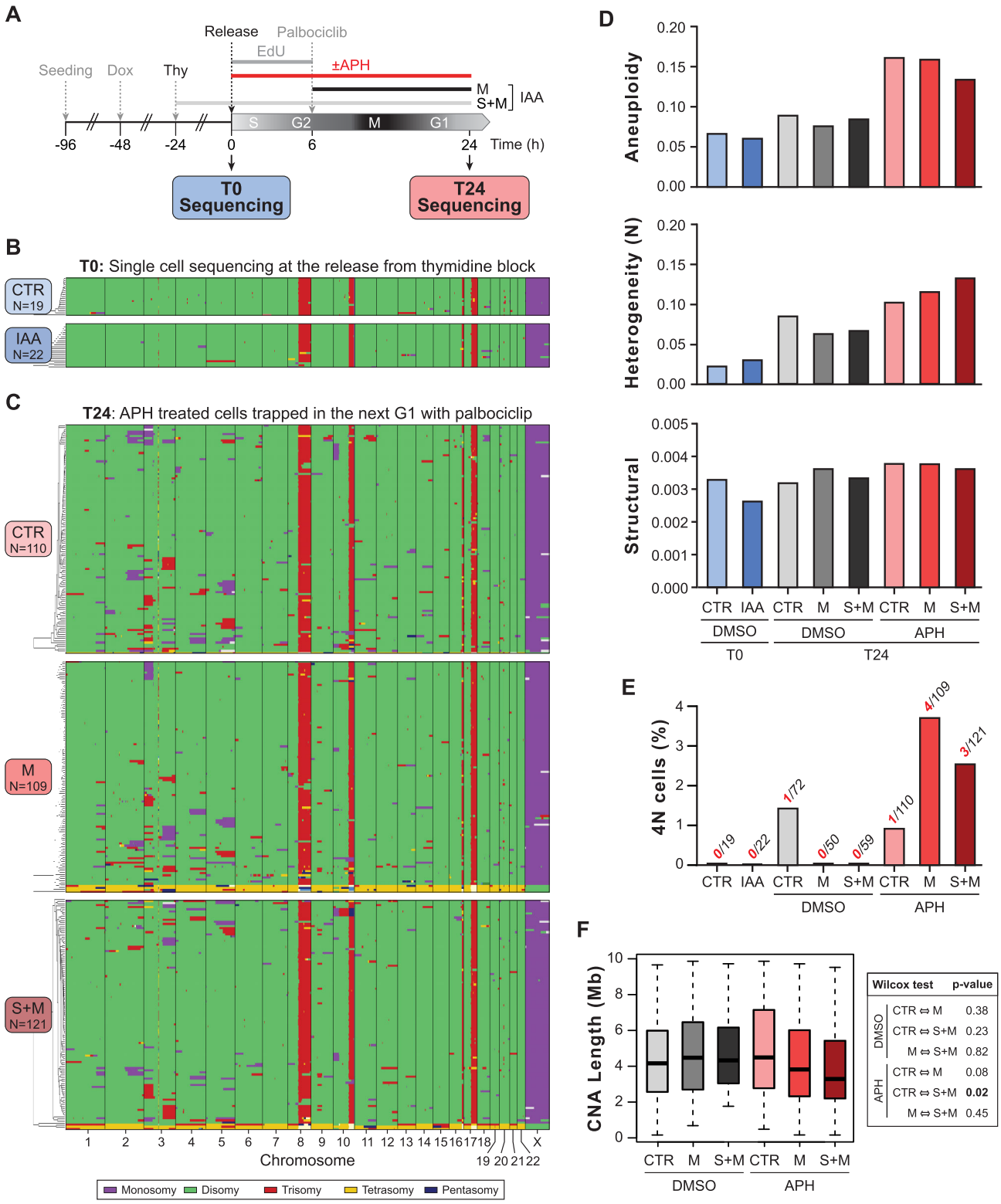

Figure 6. scWGS analysis of BLM depleted cells passing through a single S-phase in the presence or absence of APH. (**A**) Schematic illustration of the experimental strategy. APH, aphidicolin; IAA, auxin; Thy, thymidine; Dox, doxycycline. (**B** and **C**) Genome-wide copy number plots generated by the Aneufinder algorithm. Cells treated as shown in (A) were subjected to low coverage scWGS. Sequence reads were aligned to the human reference genome (GRCh38/hg38) and averaged over 1 MB nonoverlapping bins. Note that the structural chromosomal changes within t(8p;18q), 10q+, t(9q;16p-) 16q and 17q, as well as chromosome Y loss are characteristic of HCT116. Copy number plots of cells passing through an unperturbed S-phase are shown in Supplementary Fig. S9C. (**E**) Aneufinder analysis of the level of aneuploidy, heterogeneity and structural aberrations (see Materials and methods for details). (**D**) Fraction of tetrasomic cells as shown in (C). (**F**) Distribution of CNA fragment length. Results from a Wilcoxon test are shown next to the graph.

activity remain incompletely understood and represent an active area of ongoing investigation [50–52].

Another intriguing observation from our live-cell imaging is the accumulation of the BLM helicase during ana- and telophase in a few mitotic foci that also stain positive for the PICH helicase (Figs 2B and 4B). By examining their co-localization with several prototypic marker proteins, we demonstrate that the largest subset is found at centromeres. Earlier reports also demonstrated a focal accumulation of PICH near centromeres throughout mitosis [25, 51, 53]. However, in contrast to PICH, BLM localization at the centromeres is likely more transient, starting only after anaphase onset, which is critical, as uncontrolled BLM activity in metaphase cells appears to compromise centromere stability [54, 55]. While some of these foci may simply reflect remnants of resolved UFBs, they may also point to a new function of BLM and PICH at a subset of centromeres. Human centromeres are regions that replicate later in the S phase and are composed of long, AT-rich repetitive sequences with a tendency to form non-B-DNA structures and DNA:RNA hybrids [56]. Their structure makes centromeres inherently prone to DNA breakage, which is exacerbated under replication stress [57]. Recent proteomic studies revealed an enrichment of BLM and other components of UFB resolving protein complexes on centromeric DNA, potentially acting to counterbalance its fragility [43]. It therefore will be interesting to elucidate, whether and how the BLM helicase accumulating in select CENP-B positive foci late in mitosis contributes to the suppression of DNA breaks in pericentric DNA.

Using rapid, auxin-induced depletion we show that passage through a single cell cycle in the absence of the BLM helicase induces genomic instability, as evidenced by a steep increase of micronucleated cells, chromosomal breaks, and anaphase cells with UFBs (Fig. 3 and Supplementary Fig. S6C). Of note, such acute depletion eliminates selection of suppressor mutations commonly observed in BLM-deficient cells [58], which may severely confound the effects of BLM depletion on genome stability. The rapid depletion further allowed us to restrict BLM loss to a single mitosis, enabling us to study individually the contribution of early and late BLM functions to the maintenance of genome stability. Strikingly, mitotic depletion of BLM increased the number of UFBs to similar levels as in cells with continuous depletion over the entire cell cycle (Fig. 3H and Supplementary Fig. S6C). This suggests that the early BLM functions in S and G2 phase contribute only little to the suppression of UFB formation and that the accumulation of UFBs was mainly due to an impaired resolution of the sister chromatid linkages. Surprisingly, also lagging chromosomes increased to similar levels in both depletion schemes, whereas the level of micronucleation was higher in cells with continuous BLM depletion (Fig. 3E, and Supplementary Fig. S6A and B). Together with the observation that most micronuclei stained negative for the CENP-B protein, we conclude that suppression of micronucleation is driven mostly by the early BLM functions in the S and G2 phase of the cell cycle, such as the stabilization and restart of stalled replication forks [59]. These may suppress breakage of stalled replication forks and thereby prevent the formation of acentric chromosome fragments that give rise to the CENP-B negative micronuclei.

Strikingly, live-cell imaging revealed the existence of two different classes of UFBs, which can be distinguished according to their morphology and dynamics as short-lived, "straight" and long-lived "wavy" UFBs. While the proportion of cells exhibiting "wavy" UFBs clearly increased upon BLM depletion, the frequency of "straight" UFBs remained unchanged. The observation that all "straight" UFBs are rapidly resolved irrespective of BLM depletion (Fig. 4F) suggests the involvement of a redundant pathway in their resolution. The persistence of the "wavy" UFBs moreover suggests that their underlying structure differs from those of straight UFBs, making them resistant against cleavage or resolution by the back-up pathways. Additional experiments will be required to determine, how "straight" UFBs differ structurally from "wavy" UFBs, whether they are induced by distinct perturbations, and if they arise at different genomic loci.

To further investigate the consequences of acute BLM depletion on genome stability, we subjected the cells to scWGS. Similar to an earlier report [60], passage through a single cell cycle in the presence of low doses of APH caused the accumulation of a significant number of CNAs compared to synchronized cells harvested just before the release into S phase. However, except for the induction of a low number of tetraploid cells, and reduced CNA size, BLM depletion did not substantially increase the overall frequency of CNAs in our model system (Fig. 6). These results were surprising, given the synergistic effects of replication stress and BLM depletion on micronucleation, UFB frequency, as well as binucleation. The pronounced increase in DNA breaks following BLM depletion (Fig. 3G) along with the well-documented cancer predisposition associated with Bloom syndrome, raises the question of why acute BLM loss did not lead to a more pronounced genomic instability in our scWGS analysis. One possible explanation is that additional cell divisions may be necessary for accumulating measurable genome rearrangements to become established or that the most prevalent genomic alterations (e.g. translocations) remain undetectable by our short-read, low-coverage genome sequencing approach. Recently, high coverage whole genome sequencing revealed a strong increase of interchromosomal translocations in p53-deficient cells where PICH was depleted for three consecutive days [51]. Similarly, low coverage scWGS revealed a modest increase of CNAs in knock-in cells harboring patient-derived BLM mutations [61]. Taken together, we conclude that acute loss of BLM during one cell cycle does not drive the immediate accumulation of CNAs in cells challenged with mild replication stress. Instead, additional rounds of DNA damage processing over multiple cell cycles may be required to repair the lesion, leaving behind scars in the DNA. Complementary experiments will be required to fully evaluate the genomic consequences of acute BLM depletion and to understand the molecular mechanism that underlie the altered CNA size distribution. Collectively, the detection of tetraploid cells in our scWGS analysis (Fig. 6E) together with the accumulation of binucleated cells following acute BLM depletion during a single cell cycle (Fig. 4G) provides evidence that the absence of BLM depletion leads to long-lived inter-sister chromatid linkages that impair cytokinesis. These results are consistent with the accumulation of binucleated cells in chronically BLM-deficient patient cells [20] or upon siRNA-mediated depletion of BLM, PICH, or RIF1 [26, 52]. In our live-cell imaging, we observed a subset of "wavy" UFBs that persist long into telophase, coinciding with chromatin decondensation (Fig. 4D). Although we could not further track these bridges due to the release of the fluorescent marker proteins from the UFBs, they likely triggered the formation of binucleated cells, as DNA trapped at cleavage furrow interferes with abscission [62]. In support of this idea, the

post-mitotic cells with "wavy" UFBs often remained tightly connected to each other and showed symmetric sister-nuclei, a typical feature of binucleated cells. Our observations indicate that, in addition to unresolved chromatin bridges [62], persistent ultrafine bridges composed of chromatin-free DNA linkages between sister chromatids can impair abscission, leading to daughter cells that remain connected by stable intercellular canals. These findings underscore the essential role of BLM during mitosis in ensuring accurate segregation of chromatin into daughter cells and suggest that the mitotic BLM function directly supports genome stability by actively suppressing whole genome doubling, a recognized frequent driver of tumorigenesis [63]. While it is well established that the BLM helicase suppresses tumorigenesis in animal models by preventing the loss of heterozygosity through its role in homologous recombination (e.g. [64]), it remains to be determined how BLM's critical function in ensuring faithful chromosome segregation and cytokinesis contribute to this process.

Acknowledgements

We thank Masato Kanemaki for providing HCT116 cells expressing TIR1, Michael Taschner, and Stephan Gruber for providing advice and reagents for the modular cloning strategy and Andrea Tijhuis for help with cell sorting and library preparation. Biorender was used to prepare the graphical abstract and parts of Fig. 1A and Fig. 4D.

Author contribution: Conceptualization, M.R. and Z.S.; Methodology, M.R., Z.S.; Investigation, T.H., A.W., A.T., F.M., K.V., M.L., I.I.G., R.W., I.H. and F.F.; Writing – Original Draft M.R. and Z.S.; Writing – Review & Editing, all authors; Funding Acquisition, M.R., Z.S. and I.T.; Supervision, M.R., Z.S., I.T., B.W. and F.F.

Supplementary data

Supplementary data is available at NAR online.

Conflict of interest

F.F. is Chief Scientific Director of iPsomics, a startup business that provides scWGS services to the academic community. All other authors declare no conflict of interest.

Funding

This project was funded by the Deutsche Forschungsgemeinschaft (DFG) under FOR2800 Chromosome Instability: "Cross-talk of DNA replication stress and mitotic dysfunction" to Z.S. (DFG STO 918/7-2), M.R. (DFG RA 2941/2-2), by the European Research Council (ERC) Synergy Grant (GA 855158) to I.M.T., and a Dutch Cancer Society Grant (2017-RUG-11457) to F.F. Funding to pay the Open Access publication charges for this article was provided by DFG FOR2800.

Data availability

scWGS data have been deposited at the European Nucleotide Archive (ENA) and can be accessed using the following ID: PRJEB88724

References

1. German J. Bloom syndrome: a mendelian prototype of somatic mutational disease. *Medicine (Baltimore)* 1993;72:393–406. https://doi.org/10.1097/00005792-199311000-00003
2. Ellis NA, Groden J, Ye TZ *et al.* The Bloom's syndrome gene product is homologous to RecQ helicases. *Cell* 1995;83:655–66. https://doi.org/10.1016/0092-8674(95)90105-1
3. Dutertre S, Ababou M, Onclercq R *et al.* Cell cycle regulation of the endogenous wild type Bloom's syndrome DNA helicase. *Oncogene* 2000;19:2731–8. https://doi.org/10.1038/sj.onc.1203595
4. Kharat SS, Tripathi V, Damodaran AP *et al.* Mitotic phosphorylation of Bloom helicase at Thr182 is required for its proteasomal degradation and maintenance of chromosomal stability. *Oncogene* 2016;35:1025–38. https://doi.org/10.1038/onc.2015.157
5. Martin CA, Sarlos K, Logan CV *et al.* Mutations in TOP3A cause a bloom syndrome-like disorder. *Am Hum Genet* 2018;103:221–31. https://doi.org/10.1016/j.ajhg.2018.07.001
6. Gonenc II, Elcioglu NH, Martinez Grijalva C *et al.* Phenotypic spectrum of BLM- and RMI1-related Bloom syndrome. *Clin Genet* 2022;101:559–64. https://doi.org/10.1111/cge.14125
7. Bythell-Douglas R, Deans AJ. A structural guide to the bloom syndrome complex. *Structure* 2021;29:99–113. https://doi.org/10.1016/j.str.2020.11.020
8. Kaur E, Agrawal R, Sengupta S. Functions of BLM helicase in cells: is it acting like a double-edged sword? *Front Genet* 2021;12:634789. https://doi.org/10.3389/fgene.2021.634789
9. Bischof O, Kim SH, Irving J *et al.* Regulation and localization of the Bloom syndrome protein in response to DNA damage. *J Cell Biol* 2001;153:367–80. https://doi.org/10.1083/jcb.153.2.367
10. Zhong S, Hu P, Ye TZ *et al.* A role for PML and the nuclear body in genomic stability. *Oncogene* 1999;18:7941–7. https://doi.org/10.1038/sj.onc.1203367
11. Schawalder J, Paric E, Neff NF. Telomere and ribosomal DNA repeats are chromosomal targets of the bloom syndrome DNA helicase. *BMC Cell Biol* 2003;4:15. https://doi.org/10.1186/1471-2121-4-15
12. Yankiwski V, Marciniak RA, Guarente L *et al.* Nuclear structure in normal and Bloom syndrome cells. *Proc Natl Acad Sci USA* 2000;97:5214–9. https://doi.org/10.1073/pnas.090525897
13. Davalos AR, Campisi J. Bloom syndrome cells undergo p53-dependent apoptosis and delayed assembly of BRCA1 and NBS1 repair complexes at stalled replication forks. *J Cell Biol* 2003;162:1197–209. https://doi.org/10.1083/jcb.200304016
14. Tikoo S, Madhavan V, Hussain M *et al.* Ubiquitin-dependent recruitment of the Bloom syndrome helicase upon replication stress is required to suppress homologous recombination. *EMBO J* 2013;32:1778–92. https://doi.org/10.1038/emboj.2013.117
15. Eladad S, Ye TZ, Hu P *et al.* Intra-nuclear trafficking of the BLM helicase to DNA damage-induced foci is regulated by SUMO modification. *Hum Mol Genet* 2005;14:1351–65. https://doi.org/10.1093/hmg/ddi145
16. Golub EI, Gupta RC, Haaf T *et al.* Interaction of human rad51 recombination protein with single-stranded DNA binding protein, RPA. *Nucleic Acids Res* 1998;26:5388–93. https://doi.org/10.1093/nar/26.23.5388
17. Haaf T, Golub EI, Reddy G *et al.* Nuclear foci of mammalian Rad51 recombination protein in somatic cells after DNA damage and its localization in synaptonemal complexes. *Proc Natl Acad Sci USA* 1995;92:2298–302. https://doi.org/10.1073/pnas.92.6.2298
18. Balbo Pogliano C, Ceppi I, Giovannini S *et al.* The CDK1–TOPBP1–PLK1 axis regulates the Bloom's syndrome helicase BLM to suppress crossover recombination in somatic cells. *Sci Adv* 2022;8:eabk0221. https://doi.org/10.1126/sciadv.abk0221
19. Leng M, Chan DW, Luo H *et al.* MPS1-dependent mitotic BLM phosphorylation is important for chromosome stability. *Proc Natl*

Acad Sci USA 2006;103:11485–90. https://doi.org/10.1073/pnas.0601828103
20. Chan KL, North PS, Hickson ID. BLM is required for faithful chromosome segregation and its localization defines a class of ultrafine anaphase bridges. *EMBO J* 2007;26:3397–409. https://doi.org/10.1038/sj.emboj.7601777
21. Chan YW, Fugger K, West SC. Unresolved recombination intermediates lead to ultra-fine anaphase bridges, chromosome breaks and aberrations. *Nat Cell Biol* 2018;20:92–103. https://doi.org/10.1038/s41556-017-0011-1
22. Tchurikov NA, Yudkin DV, Gorbacheva MA *et al.* Hot spots of DNA double-strand breaks in human rDNA units are produced *in vivo*. *Sci Rep* 2016;6:25866. https://doi.org/10.1038/srep25866
23. Stults DM, Killen MW, Williamson EP *et al.* Human rRNA gene clusters are recombinational hotspots in cancer. *Cancer Res* 2009;69:9096–104. https://doi.org/10.1158/0008-5472.CAN-09-2680
24. Audrey A, de Haan L, van Vugt M *et al.* Processing DNA lesions during mitosis to prevent genomic instability. *Biochem Soc Trans* 2022;50:1105–18. https://doi.org/10.1042/BST20220049
25. Baumann C, Korner R, Hofmann K *et al.* PICH, a centromere-associated SNF2 family ATPase, is regulated by Plk1 and required for the spindle checkpoint. *Cell* 2007;128:101–14. https://doi.org/10.1016/j.cell.2006.11.041
26. Nielsen CF, Huttner D, Bizard AH *et al.* PICH promotes sister chromatid disjunction and co-operates with topoisomerase II in mitosis. *Nat Commun* 2015;6:8962. https://doi.org/10.1038/ncomms9962
27. Rouzeau S, Cordelieres FP, Buhagiar-Labarchede G *et al.* Bloom's syndrome and PICH helicases cooperate with topoisomerase IIalpha in centromere disjunction before anaphase. *PLoS One* 2012;7:e33905. https://doi.org/10.1371/journal.pone.0033905
28. Sarlos K, Biebricher AS, Bizard AH *et al.* Reconstitution of anaphase DNA bridge recognition and disjunction. *Nat Struct Mol Biol* 2018;25:868–76. https://doi.org/10.1038/s41594-018-0123-8
29. Bizard AH, Allemand JF, Hassenkam T *et al.* PICH and TOP3A cooperate to induce positive DNA supercoiling. *Nat Struct Mol Biol* 2019;26:267–74. https://doi.org/10.1038/s41594-019-0201-6
30. Cong L, Ran FA, Cox D *et al.* Multiplex genome engineering using CRISPR–Cas systems. *Science* 2013;339:819–23. https://doi.org/10.1126/science.1231143
31. Morawska M, Ulrich HD. An expanded tool kit for the auxin-inducible degron system in budding yeast. *Yeast* 2013;30:341–51. https://doi.org/10.1002/yea.2967
32. Natsume T, Kiyomitsu T, Saga Y *et al.* Rapid protein depletion in human cells by auxin-inducible degron tagging with short homology donors. *Cell Rep* 2016;15:210–8. https://doi.org/10.1016/j.celrep.2016.03.001
33. Vukusic K, Tolic IM. Kinetochore-centrosome feedback linking CENP-E and Aurora kinases controls chromosome congression. *Nat Commun* 2025;16:9097. https://doi.org/10.1038/s41467-025-64804-1
34. Langmead B, Salzberg SL. Fast gapped-read alignment with Bowtie 2. *Nat Methods* 2012;9:357–9. https://doi.org/10.1038/nmeth.1923
35. Jun G, Wing MK, Abecasis GR *et al.* An efficient and scalable analysis framework for variant extraction and refinement from population-scale DNA sequence data. *Genome Res* 2015;25:918–25. https://doi.org/10.1101/gr.176552.114
36. Bakker B, Taudt A, Belderbos ME *et al.* Single-cell sequencing reveals karyotype heterogeneity in murine and human malignancies. *Genome Biol* 2016;17:115. https://doi.org/10.1186/s13059-016-0971-7
37. van den Bos H, Spierings DC, Taudt AS *et al.* Single-cell whole genome sequencing reveals no evidence for common aneuploidy in normal and Alzheimer's disease neurons. *Genome Biol* 2016;17:116. https://doi.org/10.1186/s13059-016-0976-2
38. Nishimura K, Fukagawa T, Takisawa H *et al.* An auxin-based degron system for the rapid depletion of proteins in nonplant cells. *Nat Methods* 2009;6:917–22. https://doi.org/10.1038/nmeth.1401
39. Callegari A, Kueblbeck M, Morero NR *et al.* Rapid generation of homozygous fluorescent knock-in human cells using CRISPR–Cas9 genome editing and validation by automated imaging and digital PCR screening. *Nat Protoc* 2025;20:26–66. https://doi.org/10.1038/s41596-024-01043-6
40. Chaganti RS, Schonberg S, German J. A manyfold increase in sister chromatid exchanges in Bloom's syndrome lymphocytes. *Proc Natl Acad Sci USA* 1974;71:4508–12. https://doi.org/10.1073/pnas.71.11.4508
41. Bohly N, Kistner M, Bastians H. Mild replication stress causes aneuploidy by deregulating microtubule dynamics in mitosis. *Cell Cycle* 2019;18:2770–83. https://doi.org/10.1080/15384101.2019.1658477
42. Sengupta S, Robles AI, Linke SP *et al.* Functional interaction between BLM helicase and 53BP1 in a Chk1-mediated pathway during S-phase arrest. *J Cell Biol* 2004;166:801–13. https://doi.org/10.1083/jcb.200405128
43. Scelfo A, Angrisani A, Grillo M *et al.* Specialized replication mechanisms maintain genome stability at human centromeres. *Mol Cell* 2024;84:1003–20. https://doi.org/10.1016/j.molcel.2024.01.018
44. Norppa H, Falck GC. What do human micronuclei contain? *Mutagenesis* 2003;18:221–33. https://doi.org/10.1093/mutage/18.3.221
45. Minocherhomji S, Ying S, Bjerregaard VA *et al.* Replication stress activates DNA repair synthesis in mitosis. *Nature* 2015;528:286–90. https://doi.org/10.1038/nature16139
46. Osia B, Merkell A, Lopezcolorado FW *et al.* RAD52 and ERCC6L/PICH have a compensatory relationship for genome stability in mitosis. *PLoS Genet* 2024;20:e1011479. https://doi.org/10.1371/journal.pgen.1011479
47. Ke Y, Huh JW, Warrington R *et al.* PICH and BLM limit histone association with anaphase centromeric DNA threads and promote their resolution. *EMBO J* 2011;30:3309–21. https://doi.org/10.1038/emboj.2011.226
48. Roschke AV, Stover K, Tonon G *et al.* Stable karyotypes in epithelial cancer cell lines despite high rates of ongoing structural and numerical chromosomal instability. *Neoplasia* 2002;4:19–31. https://doi.org/10.1038/sj.neo.7900197
49. Miake-Lye R, Newport J, Kirschner M. Maturation-promoting factor induces nuclear envelope breakdown in cycloheximide-arrested embryos of Xenopus laevis. *J Cell Biol* 1983;97:81–91. https://doi.org/10.1083/jcb.97.1.81
50. Kong N, Liu Z, Chan YW. RIF1 suppresses the formation of single-stranded ultrafine anaphase bridges via protein phosphatase 1. *Cell Rep* 2023;42:112032. https://doi.org/10.1016/j.celrep.2023.112032
51. Kong N, Chen K, Chanboonyasitt P *et al.* The interplay of the translocase activity and protein recruitment function of PICH in ultrafine anaphase bridge resolution and genomic stability. *Nucleic Acids Res* 2025;53. https://doi.org/10.1093/nar/gkae1249
52. Hengeveld RC, de Boer HR, Schoonen PM *et al.* Rif1 Is required for resolution of ultrafine DNA bridges in anaphase to ensure genomic stability. *Dev Cell* 2015;34:466–74. https://doi.org/10.1016/j.devcel.2015.06.014
53. Sridharan V, Azuma Y. SUMO-interacting motifs (SIMs) in Polo-like kinase 1-interacting checkpoint helicase (PICH) ensure proper chromosome segregation during mitosis. *Cell Cycle* 2016;15:2135–44. https://doi.org/10.1080/15384101.2016.1191713
54. Fernández-Casañas M, Karanika E, Olukoga T *et al.* Centromere protection requires strict mitotic inactivation of the Bloom syndrome helicase complex. *Nat Commun* 2025;16:7832. https://doi.org/10.1038/s41467-025-62966-6
55. Jones Addis, O. Tiwari, A. Olukoga *et al.* PLK1 facilitates chromosome biorientation by suppressing centromere

disintegration driven by BLM-mediated unwinding and spindle pulling. *Nat Commun* 2019;10:2861. https://doi.org/10.1038/s41467-019-10938-y
56. Barra V, Fachinetti D. The dark side of centromeres: types, causes and consequences of structural abnormalities implicating centromeric DNA. *Nat Commun* 2018;9:4340. https://doi.org/10.1038/s41467-018-06545-y
57. Scelfo A, Fachinetti D. Centromere: a Trojan horse for genome stability. *DNA Repair (Amst)* 2023;130:103569. https://doi.org/10.1016/j.dnarep.2023.103569
58. Azanjac N, Milisavljevic M, Stanovcic S *et al.* Suppressors of Blm-deficiency identify three novel proteins that facilitate DNA repair in Ustilago maydis. *DNA Repair (Amst)* 2024;140:103709. https://doi.org/10.1016/j.dnarep.2024.103709
59. Davies SL, North PS, Hickson ID. Role for BLM in replication-fork restart and suppression of origin firing after replicative stress. *Nat Struct Mol Biol* 2007;14:677–9. https://doi.org/10.1038/nsmb1267
60. Shaikh N, Mazzagatti A, De Angelis S *et al.* Replication stress generates distinctive landscapes of DNA copy number alterations and chromosome scale losses. *Genome Biol* 2022;23:223. https://doi.org/10.1186/s13059-022-02781-0
61. Gönenc II, Wolff A, Busley AV *et al.* BTRR complex deficiency is a driver for genomic instability in Bloom syndrome. bioRxiv, https://doi.org/10.1101/2025.04.17.649287, 22 April 2025, preprint: not peer reviewed.
62. Steigemann P, Wurzenberger C, Schmitz MH *et al.* Aurora B-mediated abscission checkpoint protects against tetraploidization. *Cell* 2009;136:473–84. https://doi.org/10.1016/j.cell.2008.12.020
63. Bielski CM, Zehir A, Penson AV *et al.* Genome doubling shapes the evolution and prognosis of advanced cancers. *Nat Genet* 2018;50:1189–95. https://doi.org/10.1038/s41588-018-0165-1
64. Luo G, Santoro IM, McDaniel LD *et al.* Cancer predisposition caused by elevated mitotic recombination in Bloom mice. *Nat Genet* 2000;26:424–9. https://doi.org/10.1038/82548

Received: May 9, 2025. **Revised:** January 31, 2026. **Accepted:** February 10, 2026